Fault-Tolerant Wireless Power Transfer System With a Dual-Coupled LCC-S Topology

Zhengchao Yan, *Student Member, IEEE*, Yiming Zhang, *Member, IEEE*, Kehan Zhang, *Member, IEEE*, Baowei Song, Siqi Li, *Member, IEEE*, Tianze Kan, *Member, IEEE*, and Chunting Chris Mi, *Fellow, IEEE*

***Abstract*—A dual-coupled inductor-capacitor-capacitor and series (LCC-S) compensated wireless power transfer (WPT) system with a compact receiver size is proposed in this paper to improve the misalignment performance and achieve fault tolerant operation as well as a stable output power. The compensation coil and the main coil are integrated as two decoupled unipolar coils on the transmitter side, while they are both coupled with the receiver coil. The two mutual inductances among the two decoupled coils and the receiver coil have opposite impacts on the output power when they both increase or decrease. Therefore, the output power can remain stable when the misalignment increases. The short- and open-circuit characteristics are analyzed, which demonstrates that the proposed topology can achieve both short- and open-circuit protection. A prototype was built and the experimental results verified the theoretical analysis and simulations. The system can deliver from 297 W to 321 W when the x-misalignment increases from 0 mm to 90 mm, with a dc-dc efficiency of 92.78% to 93.56%. The proposed WPT system can be used for the wireless charging of e-mobility scooters and autonomous underwater vehicles. The system can provide a stable output and can tolerate both short- and open-circuit faults at the output.**

***Index Terms*—Wireless power transfer, stable output power, fault tolerant, decoupled, LCC-S.**

I. Introduction

WIRELESS power transfer (WPT) is widely used in diverse scenarios [1]–[4], such as electric vehicles (EVs), ranging from heavy buses to light electric bicycles. The research focus covers the power electronics converters, coil optimization [5], compensation topologies [6]–[8], foreign object detection [9], and safety issues [10]. Among these fields, the compensation topologies are crucial to increase the overall efficiency and minimize the volt-ampere (VA) rating of the power electronics converters by using additional inductors and capacitors to adjust the reactive power. However, the additional components increase the size, weight, and cost of the system. Therefore, the number of additional components should be as few as possible, especially for the receiver side.

The series-series (SS) topology is widely utilized due to its simplicity and constant-current output characteristic, which is good for the charging current control. In addition, the resonant frequency is independent of the coupling coefficient and the load, which is advantageous for wireless charging [11], [12]. However, the output power is inversely proportional to the coupling coefficient between the transmitter and the receiver, which results in primary-side overcurrent under the misaligned case. Also, overcurrent will happen for the SS topology with the open-circuit fault. The double-sided inductor-capacitor-capacitor (LCC-LCC) topology with its tuning method was proposed to achieve zero voltage switching (ZVS) for the switches of the primary inverter [13]. The output power of the LCC-LCC compensation topology is proportional to the coupling coefficient, which will protect the circuit during the misalignments. However, two inductors and four capacitors are introduced into the matching circuit, leading to a high cost and a large size. Moreover, the output power will decrease when the misalignment increases. The LCC-LCC topology is also not tolerant to the open-circuit fault due to its constant-current output characteristic.

In the LCC-compensated WPT systems, the compensation inductors can be integrated with the main coils, achieving a compact magnetic coupler. A method that integrated the unipolar compensation coil into the double-D (DD) main coil was proposed, realizing a compact system size and eliminating the extra coupling [14]. An integrated LCC-LCC topology was also presented to analyze the three operation modes based on the steady-state model [15].

The misalignment issue in a WPT system has been extensively studied. A WPT system with a series transmitter coil was proposed to improve the horizontal misalignment tolerance [16]. A three-phase WPT system was proposed to improve the performance during the rotational misalignment of the automatic underwater vehicle [17]. A hybrid WPT system that

Manuscript received December 10, 2018; revised April 13, 2019 and August 17, 2019; accepted September 22, 2019. Date of publication October 1, 2019; date of current version December 17, 2019. This work was supported in part by the Natural Science Basic Research Plan in the Shaanxi Province of China under Grants 2018JM5033 and 2018JQ5042, in part by the National Natural Science Foundation of China under Grant 51809214, and in part by China Scholarship Council under Grant 201706290074. The review of this article was coordinated by Prof. M. Kazerani. *(Corresponding author: Chunting Chris Mi.)*

Z. Yan is with School of Marine Science and Technology, Northwestern Polytechnical University, Xi'an 710072, China, and also with the Department of Electrical and Computer Engineering, San Diego State University, San Diego, CA 92182 USA (e-mail: yanzc1991@gmail.com).

Y. Zhang is with Maritime Institute, Nanyang Technological University, 639798 Singapore (e-mail: zhangym07@gmail.com).

K. Zhang and B. Song are with the School of Marine Science and Technology, Northwestern Polytechnical University, Xi'an 710072, China (e-mail: zhangkehan210@163.com; songbaowei@nwpu.edu.cn).

S. Li is with the School of Electrical Engineering, Kunming University of Science and Technology, Kunming 650500, China (e-mail: lisiqi@kmust.edu.cn).

T. Kan is with the ANSYS Inc., Canonsburg, PA 15317 USA (e-mail: tianze.kan@ansys.com).

C. C. Mi is with the Department of Electrical and Computer Engineering, San Diego State University, San Diego, CA 92182 USA (e-mail: mi@ieee.org).

Digital Object Identifier 10.1109/TVT.2019.2944841

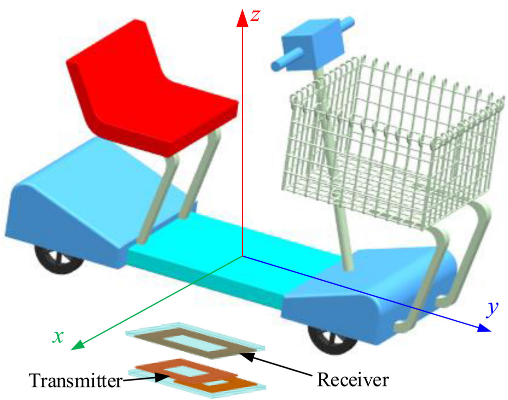

Fig. 1. General overview of the WPT system for mobility scooters.

used a combination of SS and LCC-LCC resonant networks was proposed to realize a constant charging profile over a wide range of pad misalignment [18]. Furthermore, they proposed another series-hybrid WPT system which integrated the SS and LCL networks into polarized magnetic couplers to improve the misalignment tolerance [19]. Moreover, a WPT system with the LCC-LCC compensation topology was proposed with integrated dual-coupled magnetic coupler to improve the misalignment performance [20]. However, too many passive components were introduced into the receiver side, which resulted in a high cost and a large size.

In this paper, we aim to charge mobility scooters, as shown in Fig. 1. The rated charging voltage is 48 V, and the ground clearance is around 80 mm. It is convenient to move the mobility scooters in *y* direction while it is difficult to shift in *x* direction. Therefore, we focus on solving the issue of *x*-misalignment. The dual-coupled inductor-capacitor-capacitor and series (LCC-S) compensated WPT system is proposed to make the receiver side more compact while maintaining a constant output profile when the misalignment increases. In addition, the dual-coupled LCC-S-compensated WPT system can achieve freedom from short- and open-circuit faults. The analytical model is established to analyze the system characteristics. A prototype was built to verify the analysis. Moreover, with proper coil design, the dual-coupled LCC-S-compensated WPT system can also be applied to autonomous underwater vehicles (AUVs).

II. Theoretical Analysis

A. Modeling and Derivations

The circuit topology of the proposed WPT system is depicted in Fig. 2, where the dual-coupled LCC-S topology is proposed to keep the output power constant and be free from open- and short-circuit faults. L_1 (L_2) is the transmitter (receiver) inductance, C_1 (C_2) is the series compensation capacitance, C_{f} is the parallel compensation capacitance, L_{f} is the compensation inductance, U_{bus} (U_{bat}) is the inverter dc (battery) voltage, U_1 (U_2) is the inverter (rectifier) ac voltage, I_{f} is the inverter ac current, I_1 (I_2) is the transmitter (receiver) current, and M_{f2} (M_{12}) is the mutual inductance between L_{f} (L_1) and L_2.

L_1 and L_{f} are designed to be decoupled and the mutual inductance between them is zero. L_{f} and L_2 are under different dotted terminals and L_1 and L_2 are under the same dotted terminals. Based on the Kirchhoff's law, the equations of the equivalent circuit can be expressed as

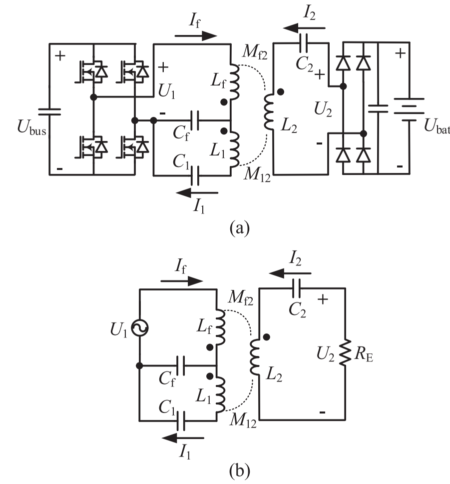

Fig. 2. The dual-coupled LCC-S-compensated WPT system. (a) Topology. (b) Equivalent circuit.

$$\begin{bmatrix} j\omega L_{\mathrm{f}} + \dfrac{1}{j\omega C_{\mathrm{f}}} & -\dfrac{1}{j\omega C_{\mathrm{f}}} & -j\omega M_{\mathrm{f2}} \\ -\dfrac{1}{j\omega C_{\mathrm{f}}} & j\omega L_1 + \dfrac{1}{j\omega C_1} + \dfrac{1}{j\omega C_{\mathrm{f}}} & j\omega M_{12} \\ -j\omega M_{\mathrm{f2}} & j\omega M_{12} & j\omega L_2 + \dfrac{1}{j\omega C_2} + R_{\mathrm{E}} \end{bmatrix} \cdot \begin{bmatrix} I_{\mathrm{f}} \\ I_1 \\ I_2 \end{bmatrix} = \begin{bmatrix} U_1 \\ 0 \\ 0 \end{bmatrix} \tag{1}$$

where ω is the operating frequency and R_{E} denotes the equivalent resistance seen before the rectifier. According to [21], R_{E} is defined as

$$R_{\mathrm{E}} = \frac{\pi^2}{8} R_{\mathrm{L}} \tag{2}$$

where R_{L} is the equivalent resistance of the battery. The input impedance Z_{in} is calculated as

$$Z_{\mathrm{in}} = \frac{U_1}{I_{\mathrm{f}}} \tag{3}$$

With the given parameters of $U_{\mathrm{bus}} = 150$ V, $L_1 = 120.1$ μH, $L_{\mathrm{f}} = 63.0$ μH, $L_2 = 88.4$ μH, $C_{\mathrm{f}} = 55.9$ nF, $C_1 = 62.1$ nF, $C_2 = 40.1$ nF, $M_{\mathrm{f2}} = 15.7$ μH, $M_{12} = 38.8$ μH, the calculated input impedance angle varying with the operating frequency under different load conditions is shown in Fig. 3. It can be seen that the input impedance angle is positive when the operating frequency is from 80 kHz to 88 kHz, which indicates that ZVS is achieved in this frequency range under different loads.

The resonant relationship is expressed as

$$j\omega_0 L_{\mathrm{f}} + \frac{1}{j\omega_0 C_{\mathrm{f}}} = 0, \quad j\omega_0 L_1 + \frac{1}{j\omega_0 C_1} + \frac{1}{j\omega_0 C_{\mathrm{f}}} = 0,$$
$$j\omega_0 L_2 + \frac{1}{j\omega_0 C_2} = 0 \tag{4}$$

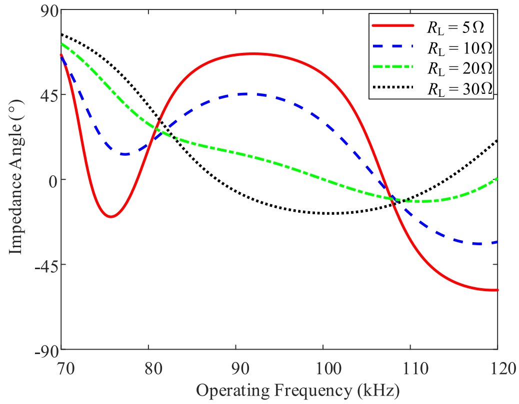

Fig. 3. The input impedance angle varying with operating frequency under different loads.

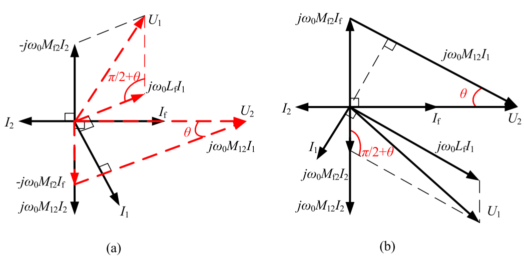

Fig. 4. Phasor diagram. (a) Different dotted terminals of L_f and L_2 used in this paper for achieving ZVS. (b) The same dotted terminals of L_f and L_2 for achieving ZCS.

where ω_0 is the resonant angular frequency. By substituting (4) into (1), it can be simplified as

$$\begin{bmatrix} 0 & j\omega_0 L_f & -j\omega_0 M_{f2} \\ j\omega_0 L_f & 0 & j\omega_0 M_{12} \\ -j\omega_0 M_{f2} & j\omega_0 M_{12} & 0 \end{bmatrix} \cdot \begin{bmatrix} I_f \\ I_1 \\ I_2 \end{bmatrix} = \begin{bmatrix} U_1 \\ 0 \\ U_2 \end{bmatrix} \tag{5}$$

Therefore, the relationship of I_f and I_2 can be expressed as

$$I_f = -\frac{M_{12}}{L_f} I_2 \tag{6}$$

The phase differences of the currents and voltages are unknown. Based on the defined directions in Fig. 2, the phasor diagram of all the ac currents and voltages is plotted in Fig. 4(a). It can be seen that U_1 leads I_f, which indicates that ZVS is achieved inherently. θ is a defined angle in the right triangle in Fig. 4(a). Zero current switching (ZCS) can also be realized easily by inversely connecting L_f and L_1, as shown in Fig. 4(b).

Based on the Pythagorean theorem and law of cosines in the triangles in Fig. 4(a), the following equations can be obtained.

$$I_1^2 = \frac{U_2^2 + (\omega_0 M_{12} I_f)^2}{(\omega_0 M_{12})^2} \tag{7}$$

$$U_1^2 = (\omega_0 M_{f2} I_2)^2 + (\omega_0 L_f I_1)^2 - 2(\omega_0 M_{f2} I_2)(\omega_0 L_f I_1)\cos\left(\frac{\pi}{2} + \theta\right) \tag{8}$$

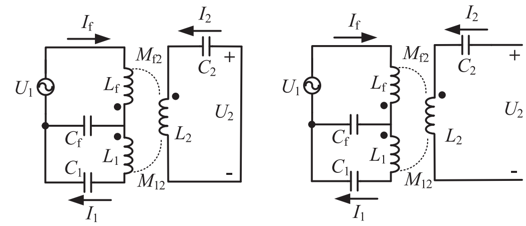

Fig. 5. Equivalent circuit. (a) Short-circuit condition. (b) Open-circuit condition.

Based on (6)–(8), I_f, I_1, and I_2 can be calculated as

$$\begin{cases} I_f = \dfrac{1}{2\omega_0 M_{f2}} \sqrt{\dfrac{M_{12}^2}{L_f^2} U_1^2 - U_2^2} \\ I_1 = \dfrac{1}{2\omega_0 M_{12}} \sqrt{\dfrac{M_{12}^2}{L_f^2} U_1^2 + 3U_2^2} \\ I_2 = \dfrac{1}{2\omega_0 M_{f2}} \sqrt{U_1^2 - \dfrac{L_f^2}{M_{12}^2} U_2^2} \end{cases} \tag{9}$$

With the Fourier Decomposition, U_1 and U_2 can be obtained as

$$U_1 = \frac{2\sqrt{2}}{\pi} U_{bus}, U_2 = \frac{2\sqrt{2}}{\pi} U_{bat} \tag{10}$$

The output power can be calculated as

$$P_{out} = U_2 I_2 = \frac{4U_{bat}}{\pi^2 \omega_0 M_{f2}} \sqrt{U_{bus}^2 - \frac{L_f^2}{M_{12}^2} U_{bat}^2} \tag{11}$$

It can be seen that M_{f2} and M_{12} have opposite impacts on P_{out} when M_{f2} and M_{12} both increase or decrease. Therefore, the output power can remain stable when the misalignment occurs.

The transfer efficiency η can be expressed as

$$\eta = \frac{P_{out}}{P_{out} + I_1^2 R_1 + I_2^2 R_2 + I_f^2 R_{Lf}} \tag{12}$$

where R_1, and R_2 denote the equivalent resistances of the transmitter and receiver and R_{Lf} represents the equivalent resistance of the compensation coil.

B. Short- and Open-Circuit Analysis

For the proposed dual-coupled LCC-S topology, it can be seen from (9) that I_2 and U_2 are coupled with each other, both dependent on U_1, which indicates that it is neither a constant-current nor a constant-voltage output. For the short-circuit fault shown in Fig. 5(a), at the steady state, $U_{2\_SC} = 0$ V. Substituting $U_{2\_SC} = 0$ V into (9) gives the short-circuit currents.

$$I_{f\_SC} = \frac{M_{12} U_1}{2\omega_0 L_f M_{f2}}, I_{1\_SC} = \frac{U_1}{2\omega_0 L_f}, I_{2\_SC} = \frac{U_1}{2\omega_0 M_{f2}} \tag{13}$$

The subscript SC stands for short-circuit. It can be noted that the short-circuit currents are within endurable values, which indicates that the WPT system is free from the short-circuit fault.

For the open-circuit fault shown in Fig. 5(b), I_{2_OC} equals zero and L_1, C_1, and C_f form a parallel resonant circuit, which

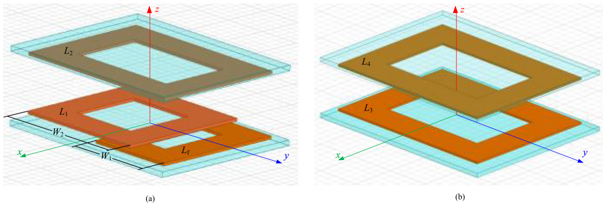

Fig. 6. (a) Proposed coil structure for dual-coupled LCC-S structure. (b) Coil structure for single-coupled LCC-S, SS, and LCC-LCC topologies.

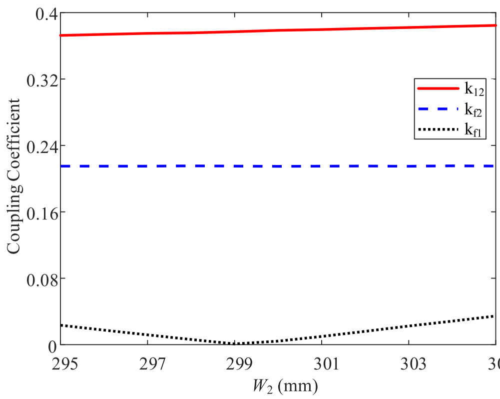

Fig. 7. Coupling coefficient versus W_2.

means I_{f_OC} is very small in this condition. Meanwhile, L_f resonates with C_f, so I_{1_OC} can be calculated as

$$I_{1\_OC} = \frac{U_1}{\omega_0 L_f} \tag{14}$$

U_{2_OC} equals the induced voltage on the receiver coil, which can be expressed as

$$U_{2\_OC} = \frac{M_{12} U_1}{L_f} \tag{15}$$

The subscript OC represents open-circuit. It can be seen that there is neither overcurrent nor overvoltage with the short- and open-circuit faults for the proposed WPT system. Therefore, the proposed dual-coupled LCC-S topology can achieve both short-circuit and open-circuit protection with no complex control method, which is helpful in the practical applications.

III. Topology Comparison

A. Coil Design

The proposed coil structure for the dual-coupled LCC-S topology is shown in Fig. 6(a), where two decoupled unipolar coils are adopted in the transmitter side, one is L_f and the other is L_1. W_1 stands for the width of L_f and W_2 denotes the width of L_1. We fix W_1 at 200 mm and adjust W_2 to find the decoupled point. In the practical application of charging mobility scooters, it is convenient to move in y direction while it is difficult to shift in x direction. Therefore, we focus on solving the issue of the x-misalignment. Fig. 7 shows the coupling coefficient

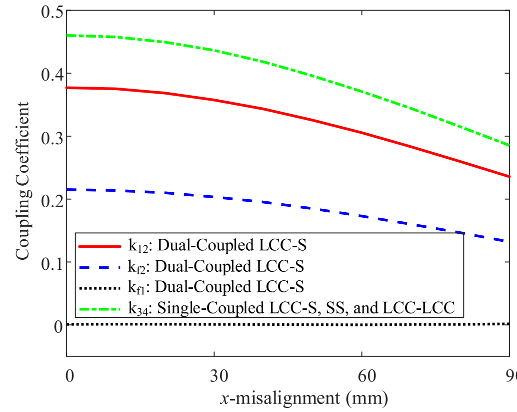

Fig. 8. Coupling coefficients varying with the x-misalignment.

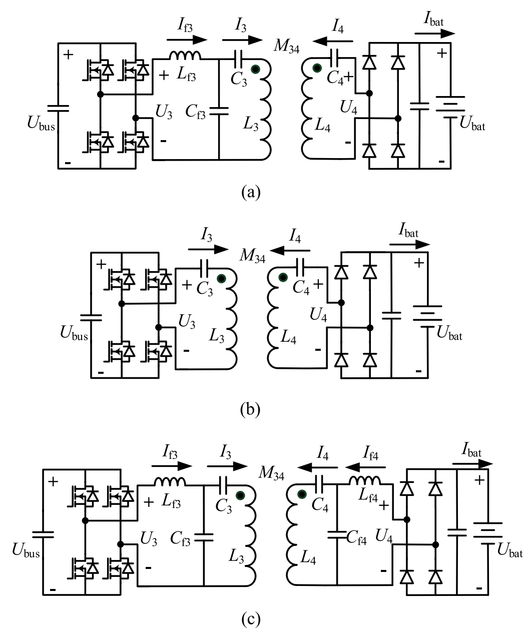

Fig. 9. Three topologies. (a) Single-coupled LCC-S. (b) SS. (c) LCC-LCC.

varying with the increasing W_2. It can be seen that L_f and L_1 are decoupled when W_2 equals 299 mm.

Fig. 6(b) shows the coil structure for single-coupled LCC-S, SS, and LCC-LCC topologies, where the transmitter and receiver coils are the same as the receiver coil of the proposed coil structure. L_3 (L_4) is the self-inductance of the transmitter (receiver). W_2 is fixed at 299 mm to achieve decoupled L_f and L_1. The coupling coefficients of the two structures are shown in Fig. 8. It indicates that the coupling coefficients between the transmitter side and the receiver side of the two structures both have a 38% decrease. For the proposed dual-coupled structure, the coupling coefficient between L_f and L_1 is small enough to be neglected.

B. Output Power

The single-coupled LCC-S, SS, and LCC-LCC topologies are shown in Fig. 9. C_3 (C_4) is the series compensation capacitance,

C_{f3} is the parallel compensation capacitance, L_{f3} (L_{f4}) is the compensation inductance, U_3 (U_4) is the inverter (rectifier) ac voltage, I_{f3} (I_{f4}) is the inverter (rectifier) ac current, I_3 (I_4) is the transmitter (receiver) current, I_{bat} is the battery current, and M_{34} is the mutual inductance between L_3 and L_4.

For the single-coupled LCC-S topology shown in Fig. 9(a), U_4 at resonance can be calculated as

$$U_4 = \frac{M_{34}U_3}{L_{f3}} \tag{16}$$

It can be seen that the single-coupled LCC-S topology has a constant-voltage output. When the battery current is I_{bat}, the output power is

$$P_{\mathrm{out\_LCC-S}} = \frac{8M_{34}U_{\mathrm{bus}}I_{\mathrm{bat}}}{\pi^2 L_{f3}} \tag{17}$$

The output power is proportional to the coupling and it will have a power decrease when the misalignment occurs.

For the SS topology shown in Fig. 9(b), the rectifier ac current at resonance is

$$I_4 = \frac{U_3}{\omega_0 M_{34}} \tag{18}$$

The SS topology has a constant-current output. The output power can be expressed as

$$P_{\mathrm{out\_SS}} = \frac{8U_{\mathrm{bus}}U_{\mathrm{bat}}}{\pi^2 \omega_0 M_{34}} \tag{19}$$

It can be seen that the output power of the SS topology is inversely proportional to the coupling.

For the LCC-LCC topology shown in Fig. 9(c), the rectifier ac current at resonance is

$$I_{f4} = \frac{M_{34}U_3}{\omega_0 L_{f3}L_{f4}} \tag{20}$$

The LCC-LCC topology also has a constant-current output. The output power at resonance is

$$P_{\mathrm{out\_LCC-LCC}} = \frac{8M_{34}U_{\mathrm{bus}}U_{\mathrm{bat}}}{\pi^2 \omega_0 L_{f3}L_{f4}} \tag{21}$$

It can be noted that the output power of the LCC-LCC topology is proportional to the coupling.

The normalized output power of the proposed dual-coupled LCC-S, single-coupled LCC-S, SS, and LCC-LCC topologies varying with the x-misalignment is shown in Fig. 10. It can be seen that when the x-misalignment increases from 0 mm to 90 mm, the output power of the SS topology increases by 61%. The output power of the LCC-LCC topology and the single-coupled LCC-S has the same trend and both decreases by 38%. In comparison, the output power of the proposed dual-coupled LCC-S topology remains stable, which is superior to the other three topologies.

C. Short- and Open-Circuit Analysis

The single-coupled LCC-S topology has a constant-voltage output. For the short-circuit fault, U_4 will remain stable, resulting in overcurrent in the secondary circuit, which requires very large I_{f3} to supply power. Therefore, the inverter and the rectifier will be damaged. While for the open-circuit fault, the I_4 and I_{f3} are zero, and I_3 remains constant, and the circuit can be protected in this condition.

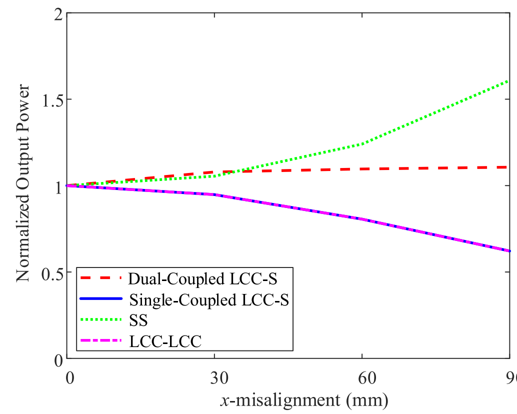

Fig. 10. Normalized output power versus the x-misalignment of the four topologies.

TABLE I
COMPARISON OF DIFFERENT TOPOLOGIES

Topology	Dual-coupled LCC-S	Single-coupled LCC-S	SS	LCC-LCC
Constant Power	✓			
Open-circuit protection	✓	✓		
Short-circuit protection	✓		✓	✓
Number of components	✓	✓	✓✓	

The SS topology has a constant-current output. For the short-circuit fault, I_4 will not change for the constant-current output characteristic, while I_3 will be very small considering the equivalent resistances of the coils, which can protect the circuit from overcurrent. However, for the open-circuit fault, I_4 is zero, resulting in overcurrent in the primary circuit.

The LCC-LCC topology also has a constant-current output. For the short-circuit fault, I_{f3} and I_4 will be zero, while the I_3 and I_{f4} remain stable due to the constant-current characteristic, which are advantageous for the circuit. However, for the open-circuit fault, I_{f4} is zero, and I_{f3} and I_4 will be very large, leading to a large voltage on C_{f4}, which will cause overvoltage in the rectifier [15].

The comparison of the dual-coupled LCC-S, single-coupled LCC-S, SS, and LCC-LCC topologies is listed in Table I. It can be seen that the proposed dual-coupled LCC-S topology can remain the constant output power during the misalignment; moreover, there is neither overcurrent nor overvoltage under the open- and short-circuit faults. Therefore, the proposed dual-coupled LCC-S topology can achieve both short-circuit and open-circuit protection with no complex control method, which is helpful in the practical applications.

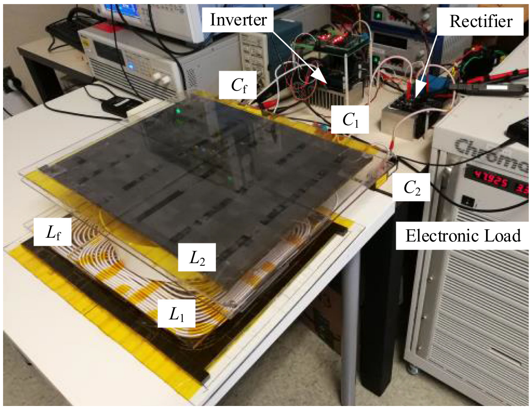

Fig. 11. Experimental prototype.

TABLE II
SYSTEM SPECIFICATIONS AND CIRCUIT PARAMETERS

U_{bus}	U_{bat}	L_f	L_1	L_2	M_{f1}
150V	48V	63.0μH	120.1μH	88.4μH	0.5μH
M_{f2}	M_{12}	C_f	C_1	C_2	f_0
15.7μH	38.8μH	55.9nF	62.1nF	40.1nF	84.6kHz

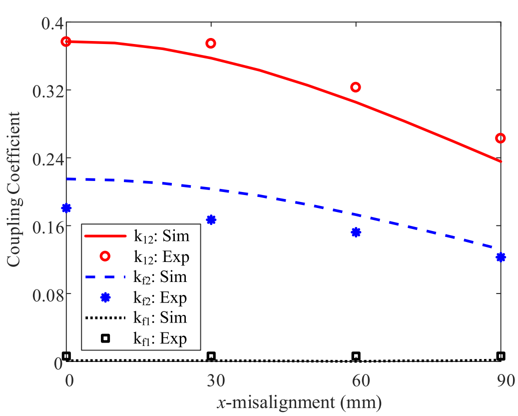

Fig. 12. Simulated and measured coupling coefficients.

IV. EXPERIMENTAL VERIFICATION

A prototype based on the proposed dual-coupled LCC-S topology is implemented, shown in Fig. 11. The system specifications and the circuit parameters with no misalignment are listed in Table II. The total outer dimension of L_f and L_1 is the same as L_2. The coils are all composed of American Wire Gauge (AWG) 38 Litz wires with 3.9 mm diameter. L_f has 12 turns, L_1 has 14 turns, and L_2 has 10 turns. The gap between the transmitter and the receiver is 80 mm. In the experiments, the x-misalignment is adjusted from 0 mm to 90 mm.

Fig. 12 shows the simulated and measured coupling coefficients varying with the x-misalignment. The coupling becomes weaker with the increasing misalignments. The measured coupling coefficients match the simulated ones well. The discrepancies between the measurements and the simulations may be caused by the parameter inaccuracy.

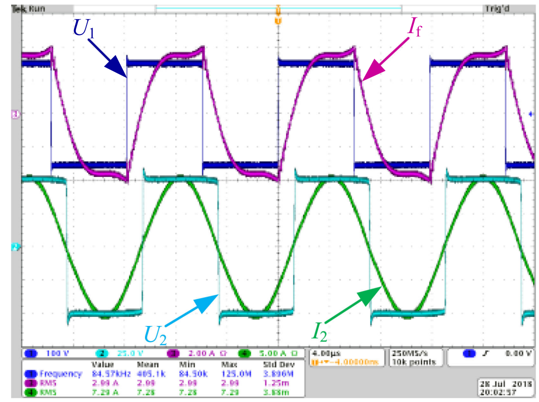

Fig. 13. Voltage and current waveforms when $U_{bus} = 150$ V and $U_{bat} = 48$ V.

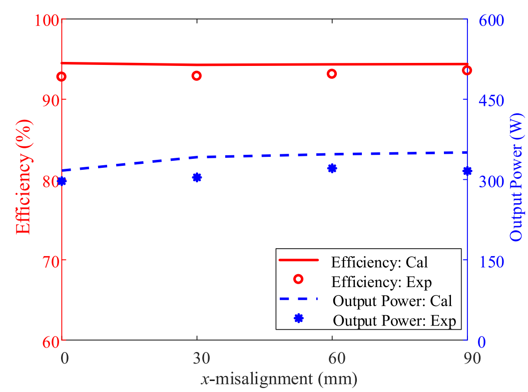

Fig. 14. DC-DC efficiency and output power versus the x-misalignment.

The experimental voltage and current waveforms are shown in Fig. 13. It can be seen that ZVS is achieved, which verifies the analysis in Section II-A, Fig. 4(a). The dc-dc efficiency and the output power varying with the x-misalignment are shown in Fig. 14. The efficiency and the output power remain relatively stable with the increasing x-misalignment. The experimental results are slightly lower than the calculated ones. It is because the switching loss of the inverter and the resistances of the compensation capacitors are not considered in the calculation. The system can deliver 297 W to 321 W when the x-misalignment increases from 0 mm to 90 mm, with a dc-dc efficiency of 92.78% to 93.56%. The experimental results agree with the calculated ones.

The short- and open-circuit characteristics of the dual-coupled LCC-S topology are shown in Fig. 15. In the short-circuit situation shown in Fig. 15(a), (b), and (c), I_f and I_2 have a small increase and I_1 decreases slightly compared to the rated output, which indicates that the circuit can be protected at the short-circuit condition. In open-circuit situation shown in Fig. 15(d), I_1 has a slight increase compared to the rated output and U_2 remains a reasonable value. The experimental

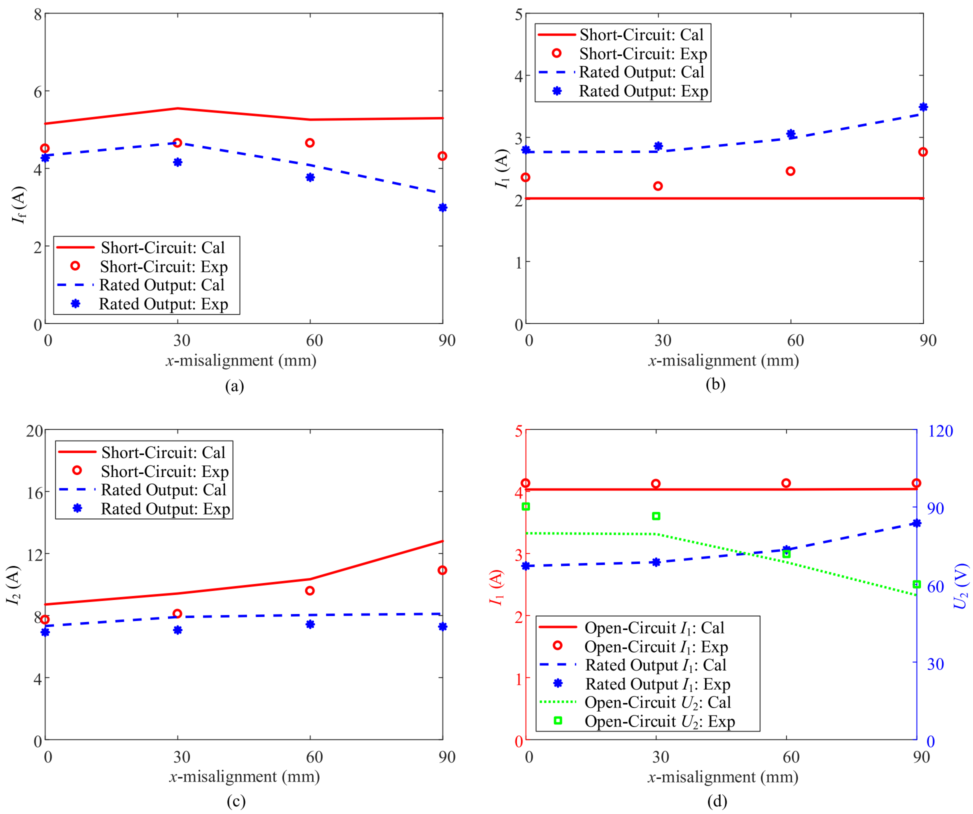

Fig. 15. RMS currents and voltages of different modes. (a) I_{f}. (b) I_1. (c) I_2. (d) I_1 and U_2.

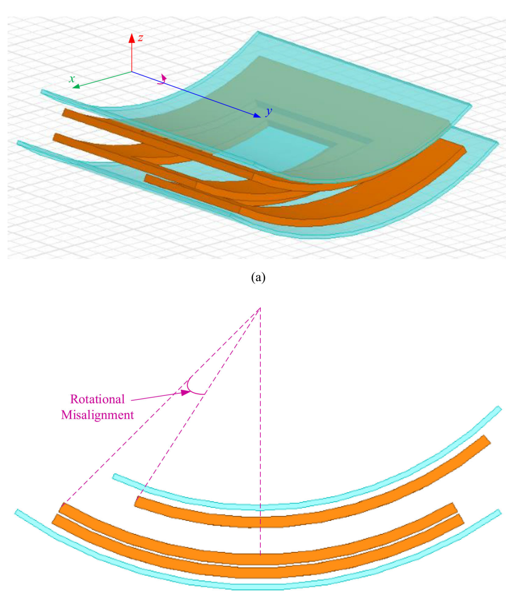

Fig. 16. (a) Proposed coil structure for dual-coupled LCC-S structure. (b) Front view of the coil structure.

results agree with the calculated ones. Therefore, the proposed dual-coupled LCC-S topology can achieve both short-circuit and open-circuit protection with no complex control method, which is helpful in the practical applications.

With proper coil design, the dual-coupled LCC-S-compensated WPT system can also be applied to AUVs, as shown in Fig. 16(a). The rotational misalignment will appear when the AUV rotates along the y axis caused by the ocean current impact, as shown in Fig. 16(b). Based on the former analysis of the dual-coupled LCC-S-compensated WPT system, the influence caused by the rotational misalignment will be significantly decreased. Therefore, this will help to better design the underwater WPT system for AUVs.

V. Conclusion

A dual-coupled LCC-S-compensated WPT system for charging the mobility scooters was proposed. The LCC compensation is adopted in the transmitter side. The compensation coil and the main coil are integrated as two decoupled unipolar coils, while they are both coupled with the receiver coil. The series compensation is used in the receiver side to achieve a compact receiver. The two mutual inductances among the two decoupled coils on the transmitter side and the receiver coil have opposite impacts on the output power when they both increase or decrease. Therefore, the output power can remain stable when the misalignment increases. The short- and open-circuit characteristics have been analyzed, which demonstrates that the proposed topology can achieve both short- and open-circuit protection. A prototype was built and the experimental results verified the theoretical analysis and simulations. The system can deliver 297 W to 321 W when the x-misalignment increases from 0 mm to 90 mm, with a dc-dc efficiency of 92.78% to 93.56%. With proper coil design, the dual-coupled LCC-S-compensated WPT system can also be applied to AUVs.

REFERENCES

[1] Z. C. Yan *et al.*, "Frequency optimization of a loosely coupled underwater wireless power transfer system considering eddy current loss," *IEEE Trans. Ind. Electron.*, vol. 66, no. 5, pp. 3468–3476, May 2019.

[2] Y. M. Zhang, T. Z. Kan, Z. C. Yan, Y. H. Mao, Z. X. Wu, and C. C. Mi, "Modeling and analysis of series-none compensation for wireless power transfer systems with a strong coupling," *IEEE Trans. Power Electron.*, vol. 34, no. 2, pp. 1209–1215, Feb. 2019.

[3] H. Z. Beh, G. A. Covic, and J. T. Boys, "Wireless fleet charging system for electric bicycles," *IEEE J. Emerg. Sel. Topics Power Electron.*, vol. 3, no. 1, pp. 75–86, Mar. 2015.

[4] R. K. Mai, Y. Chen, Y. Li, Y. Y. Zhang, G. Z. Cao, and Z. Y. He, "Inductive power transfer for massive electric bicycles charging based on hybrid topology switching with a single inverter," *IEEE Trans. Power Electron.*, vol. 32, no. 8, pp. 5897–5906, Aug. 2017.

[5] S. Kim, G. A. Covic, and J. T. Boys, "Comparison of tripolar and circular pads for IPT charging systems," *IEEE Trans. Power Electron.*, vol. 33, no. 7, pp. 6093–6103, Jul 2018.

[6] J. L. Villa, J. Sallan, J. F. S. Osorio, and A. Llombart, "High-misalignment tolerant compensation topology for ICPT systems," *IEEE Trans. Ind. Electron.*, vol. 59, no. 2, pp. 945–951, Feb. 2012.

[7] W. Zhang and C. C. Mi, "Compensation topologies of high-power wireless power transfer systems," *IEEE Trans. Veh. Technol.*, vol. 65, no. 6, pp. 4768–4778, Jun. 2016.

[8] C. S. Wang, G. A. Covic, and O. H. Stielau, "Investigating an LCL load resonant inverter for inductive power transfer applications," *IEEE Trans. Power Electron.*, vol. 19, no. 4, pp. 995–1002, Jul. 2004.

[9] S. Y. Jeong, H. G. Kwak, G. C. Jang, S. Y. Choi, and C. T. Rim, "Dual-purpose non-overlapping coil sets as metal object and vehicle position detections for wireless stationary EV chargers," *IEEE Trans. Power Electron.*, vol. 33, no. 9, pp. 7387–7397, Sep. 2017.

[10] K. H. Zhang, L. N. Du, Z. B. Zhu, B. W. Song, and D. M. Xu, "A normalization method of delimiting the electromagnetic hazard region of a wireless power transfer system," *IEEE Trans. Electromagn. Compat.*, vol. 60, no. 4, pp. 829–839, Aug. 2018.

[11] Y. Zhang, *Key Technologies of Magnetically-Coupled Resonant Wireless Power Transfer*. Berlin, Germany: Springer, 2017.

[12] S. Valtchev, B. Borges, K. Brandisky, and J. B. Klaassens, "Resonant contactless energy transfer with improved efficiency," *IEEE Trans. Power Electron.*, vol. 24, no. 3, pp. 685–699, Mar. 2009.

[13] S. Q. Li, W. H. Li, J. J. Deng, T. D. Nguyen, and C. C. Mi, "A double-sided LCC compensation network and its tuning method for wireless power transfer," *IEEE Trans. Veh. Technol.*, vol. 64, no. 6, pp. 2261–2273, Jun. 2015.

[14] T. Kan, T. D. Nguyen, J. C. White, R. K. Malhan, and C. C. Mi, "A new integration method for an electric vehicle wireless charging system using LCC compensation topology: Analysis and design," *IEEE Trans. Power Electron.*, vol. 32, no. 2, pp. 1638–1650, Feb. 2017.

[15] W. H. Li, H. Zhao, S. Q. Li, J. J. Deng, T. Z. Kan, and C. C. Mi, "Integrated LCC compensation topology for wireless charger in electric and plug-in electric vehicles," *IEEE Trans. Ind. Electron.*, vol. 62, no. 7, pp. 4215–4225, Jul. 2015.

[16] Y. Chen, R. Mai, Y. Zhang, M. Li, and Z. He, "Improving misalignment tolerance for IPT system using a third-coil," *IEEE Trans. Power Electron.*, vol. 34, no. 4, pp. 3009–3013, Apr. 2019.

[17] T. Z. Kan, Y. M. Zhang, Z. C. Yan, P. P. Mercier, and C. C. Mi, "A rotation-resilient wireless charging system for lightweight autonomous underwater vehicles," *IEEE Trans. Veh. Technol.*, vol. 67, no. 8, pp. 6935–6942, Aug. 2018.

[18] L. Zhao, D. J. Thrimawithana, and U. K. Madawala, "Hybrid bidirectional wireless EV charging system tolerant to pad misalignment," *IEEE Trans. Power Electron.*, vol. 64, no. 9, pp. 7079–7086, Sep. 2017.

[19] L. Zhao, D. J. Thrimawithana, U. K. Madawala, A. P. Hu, and C. C. Mi, "A misalignment-tolerant series-hybrid wireless EV charging system with integrated magnetics," *IEEE Trans. Power Electron.*, vol. 34, no. 2, pp. 1276–1285, Feb. 2019.

[20] F. Lu, H. Zhang, H. Hofmann, W. C. Su, and C. T. C. Mi, "A dual-coupled LCC-compensated IPT system with a compact magnetic coupler," *IEEE Trans. Power Electron.*, vol. 33, no. 7, pp. 6391–6402, Jul. 2018.

[21] W. Zhang, S. C. Wong, C. K. Tse, and Q. H. Chen, "Analysis and comparison of secondary series- and parallel-compensated inductive power transfer systems operating for optimal efficiency and load-independent voltage-transfer ratio," *IEEE Trans. Power Electron.*, vol. 29, no. 6, pp. 2979–2990, Jun. 2014.

Zhengchao Yan (S'18) received the B.S. degree in mechanical design, manufacturing and automation in 2013 from Northwestern Polytechnical University, Xi'an, China, where he is currently working toward the Ph.D. degree. He was a Joint Ph.D. Student with San Diego State University, San Diego, CA, USA, from 2017 to 2019. His research interests focus on wireless power transfer, including electromagnetic field calculation, coil design, and compensation topologies.

Yiming Zhang (S'13–M'16) received the B.S. and Ph.D. degrees in electrical engineering from Tsinghua University, Beijing, China, in 2011 and 2016, respectively. He is currently a Research Fellow with Nanyang Technological University, Singapore. His research interests include wireless power transfer for electric vehicles and mobile phones, and resonant converters.

Kehan Zhang (M'18) was born in Shaanxi, China, in 1971. He received the Ph.D. degree in Xi'an Jiaotong University, Xi'an, China, in 2000. He is currently an Associate Professor and the Master Instructor with Northwestern Polytechnical University, Xi'an, China. His research interests focus on DSP-based brushless dc motor control system and wireless power transfer.

Baowei Song received the B.S. and Ph.D. degrees in mechatronic engineering from Northwestern Polytechnical University, Xi'an, China, in 1999 and 1986, respectively. He is currently a Professor and the Vice-President of Northwestern Polytechnical University. His research interests include general technical research of underwater vehicles.

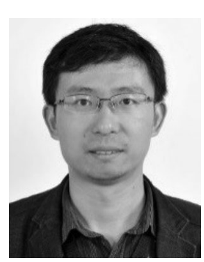

Siqi Li (M'11) received the B.S. and Ph.D. degrees in electrical engineering from Tsinghua University, Beijing, China, in 2004 and 2010, respectively. He was a Postdoctoral Fellow with the University of Michigan, Dearborn, MI, USA, from 2011 to 2013. In 2013, he joined the Faculty of Electric Power Engineering, Kunming University of Science and Technology (KUST), Kunming, China, where he is currently an Associate Professor with the Department of Electrical Engineering. Also, he is the Director of the Advanced Power Electronics and New Energy Laboratory, KUST. Since 2018, he has been a Visiting Scholar with the San Diego State University, San Diego, CA, USA. His research interest focuses on battery management system, high-performance wired, wireless battery chargers for electric vehicles, and solid state transformers.

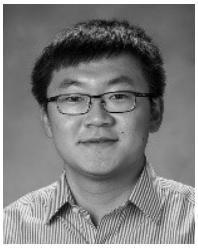

Tianze Kan (S'15–M'19) received the B.Eng. degree in electrical engineering and automation from the Huazhong University of Science and Technology, Wuhan, China, in 2011, the M.S. degree in electrical engineering from the University of Southern California, Los Angeles, CA, USA, in 2013, and the Ph.D. degree in electrical and computer engineering in the joint doctoral program between San Diego State University, San Diego, CA, USA, and the University of California San Diego, La Jolla, CA, USA, in 2018. He is currently an Application Engineer with ANSYS Inc., Canonsburg, PA, USA, where he supports simulations on low frequency electromagnetics and power electronics. His research interests include power electronics and inductive-based wireless power transfer.

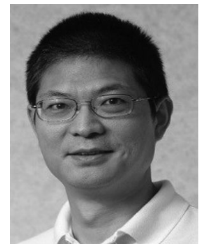

Chunting Chris Mi (S'00–A'01–M'01–SM'03–F'12) received the B.S.E.E. and M.S.E.E. degrees in electrical engineering from Northwestern Polytechnical University, Xi'an, China, in 1985 and 1988, respectively, and the Ph.D. degree in electrical engineering from the University of Toronto, Toronto, ON, Canada, in 2001. He is currently a Professor and a Chair of electrical and computer engineering and the Director of the Department of Energy (DOE) -funded Graduate Automotive Technology Education (GATE) Center for Electric Drive Transportation, San Diego State University, San Diego, USA. Prior to joining SDSU, he was with the University of Michigan, Dearborn, from 2001 to 2015. His research interests include electric drives, power electronics, electric machines, renewable-energy systems, and electric and hybrid vehicles.